Local Atmospheric Responses to Ocean Dynamic Features in the South China Sea

9

Zhe-Wen Zheng*,¶, Yi-Chun Kuo†, Chung-Ru Ho‡, Quanan Zheng§ and Nan-Jung Kuo‡

*Institute of Marine Environmental Science and Technology & Department of Earth Science, National Taiwan Normal University, Taipei, Taiwan
†Institute of Oceanography, National Taiwan University, Taipei, Taiwan
‡Department of Marine Environmental Informatics, National Taiwan Ocean University, Keelung, Taiwan
§Department of Atmospheric and Oceanic Science, University of Maryland, College Park, MD, USA
¶zwz@ntnu.edu.tw

Kuroshio intrusion within the Luzon Strait, which enters the northern South China Sea (SCS), and offshore cool-jet occurring off east Vietnam in summer are two well-documented dynamic oceanic features within the SCS. Given the possible impacts of those distinct and dynamic features on the local atmospheric environment, weather system, oceanic environment and also ecosystem, it needs to be further understood whether the sea surface variability resulting from those distinct ocean dynamic features would cause great influences feeding back to local atmosphere under certain situations. In this chapter, we will reveal the local atmospheric responses to those dynamic features, which might shed light on further improving the prediction of local weather system in the SCS. Additionally, generated mechanisms of those atmospheric responses are also analyzed.

9.1 Introduction

The Kuroshio is a western boundary current of the North Pacific Ocean. It forms in the North Equatorial Current (NEC) bifurcation region (12–18°N), where the NEC divides into two branches as it approaches the Philippine coast [Nitani, 1972]. The north branch is Kuroshio. As shown in Figure 9.1, in general, the Kuroshio main stream flows northward along the east coast of the Philippines and passes through the Luzon Strait, arriving at the south-east corner of the Taiwan Island later. Occasionally, it might turn westward and cause a distinct intrusion within the Luzon Strait, which enters the northern South China Sea (SCS).

The SCS is the largest marginal basin with a central part exceeding 4000 m in depth [Gong *et al*., 1992]. The SCS is connected to the west North Pacific Ocean via the wide and deep Luzon Strait [Metzger and Hurlbut, 1996]. It is influenced significantly by the Kuroshio, in particular, while

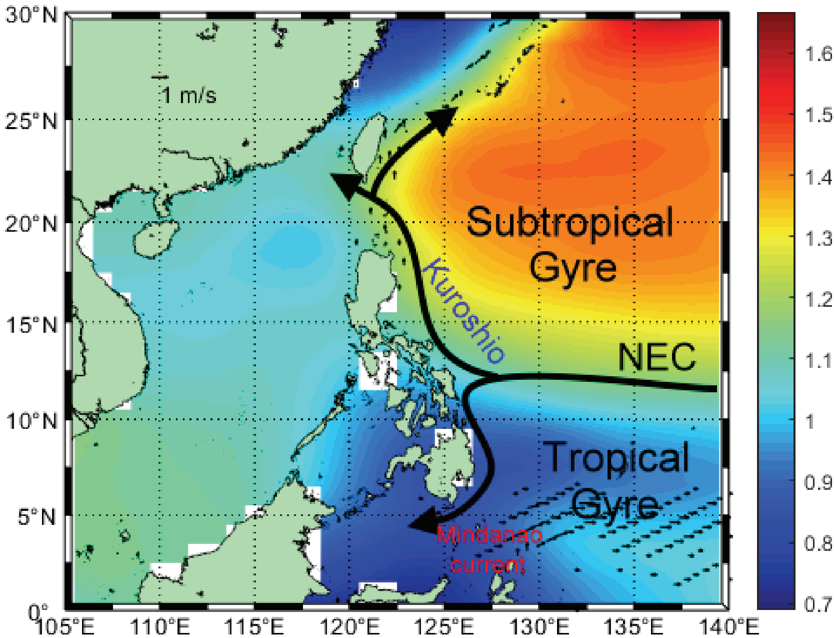

Fig. 9.1. Mean absolute dynamic topography (ADT) (cm) and the corresponding surface geostrophic currents (m s^{-1}) derived from the satellite altimeter data in 2003. Black solid lines represent a schematic of the North equatorial, Mindanao, and Kuroshio current system.

the Kuroshio intrusion occurred. As noted in Nan *et al.* [2015], Kuroshio intrusion makes important contributions to the momentum, heat and salt budgets in the SCS. In the past decades, much work has been done toward understanding of the characteristics, hydrography and distributions of the Kuroshio intrusion [Farris and Wimbush, 1996; Caruso *et al*., 2006; Chen *et al*., 2011; Nan *et al*., 2011, 2015; Hsin *et al*., 2012]. In this chapter, despite the dynamics and generations of the Kuroshio intrusion events, we focus on the atmospheric response to occurrences of the Kuroshio intrusion within the Luzon Strait.

Tight relationships of upper ocean dynamic features with consequential atmospheric processes have been well documented by previous studies [Xie, 2004; Chelton and Xie, 2010; Frenger *et al*., 2013; Chow *et al*., 2015; Oey *et al*., 2015]. For example, Frenger *et al.* [2013] indicated the drastic responses of winds, clouds and rainfall to eddies in the southern oceans. Figure 3 in Frenger *et al.* [2013] shows the schematic plots of how eddies trigger responses of local weather, including winds, clouds and rainfall. Additionally, Chow *et al.* [2015] showed the relationship between the Kuroshio intrusion off northeast Taiwan onto the East China Sea continental shelf and the consequential enhanced precipitation. They suggested that the possibility of improved weather prediction can be reached by considering the ocean variability. Meanwhile, previous investigations also indicated that changes in local winds may have an important role in determining the climate in coastal regions, because they influence the characteristic air flow, precipitation, humidity and even pollutant transports [Anthes, 1978; Kousky, 1980; Lu and Turco, 1994; Franchito, 1998]. Based on aforementioned reasons, it is more than essential to clarify the relationship between those distinct oceanic dynamic features and the consequential atmospheric responses. Nevertheless, in addition to a series of studies focused on the mechanism leading to the Kuroshio intrusion [Wang and Chern, 1987; Farris and Wimbush, 1996; Metzger and Hurlburt, 2001; Wang *et al*., 2006; Kuehl and Sheremet, 2009; Wu and Hsin, 2012], the study on possible atmospheric response triggered by the distinct oceanic features, i.e., the Kuroshio intrusion, has attracted little attention, thus possible feedbacks resulting from the dynamic Kuroshio intrusion back to the regional weather system remain unclear.

On the other hand, there is another marked oceanic feature also appearing in the SCS, which is the distinct cool-jet off east Vietnam (CJEV) [Kuo *et al*., 2000; Xie, 2004], as shown in Figure 9.2. Coastal upwelling

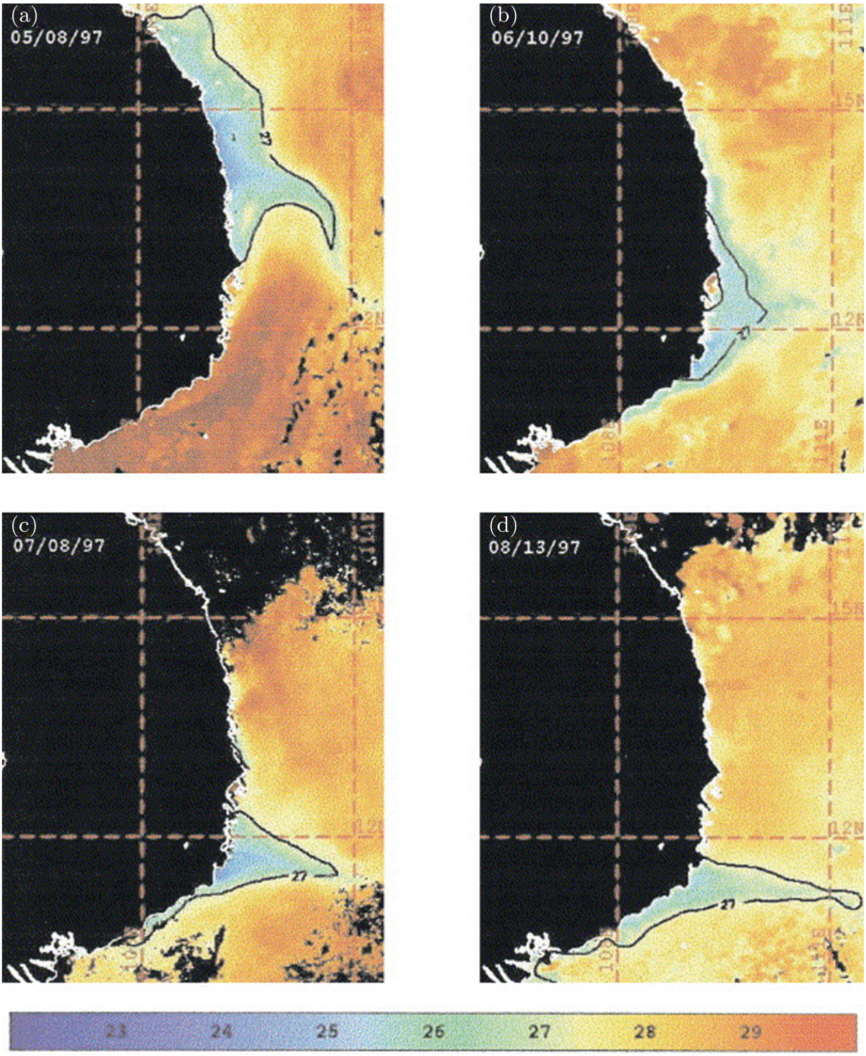

Fig. 9.2. AVHRR IR images of the western boundary of the SCS taken on (a) 8 May, (b) 10 June, (c) 8 July and (d) 13 August 1997. The offshore boundary of the cold water region on each image is enclosed with the SST contour of 27°C.

Source: Taken from Kuo *et al.* [2000].

off southeastern Vietnam leading to marked temperature drop off eastern Vietnam has been well investigated by previous studies [Ho *et al.*, 2000; Kuo *et al.*, 2000; Xie *et al.*, 2003; Xie, 2004]. Using National Oceanic and Atmospheric Administration (NOAA) satellite Advanced Very High Resolution

Radiometer (AVHRR) infrared (IR) sea surface temperature (SST) images, Kuo *et al.* [2000] showed a coastal upwelling along southern Vietnam and a cold filament that stretches eastward at about 12°N from the coast. Xie *et al.* [2003] indicated that the southwesterly wind jet plays a key role in triggering the development of the offshore cold filament, by inducing coastal upwelling and driving the eastward ocean jet that transports the cold coastal water off-shoreward. Moreover, Xie *et al.* [2003] further indicated the importance of strong intraseasonal variability in wind fields and thus the consequential development of offshore cool-jets. Their results showed that the development of the wind jet and CJEV is not a smooth seasonal process, but consists of several intraseasonal events each year at about 45-day intervals.

Overall, the general characteristics of CJEV and the Kuroshio intrusion have been well investigated [Kuo *et al.*, 2000, 2004; Xie *et al.*, 2003, 2007; Nan *et al.*, 2015]. However, it needs to be further understood whether the SST variability resulting from those distinct ocean dynamic features causes great influences feeding back to local atmosphere under certain situations. Given the possible impacts of those extra responses on the local weather system, ocean environment and ecosystem, this chapter presents possible atmospheric responses to the Kuroshio intrusion and CJEV located in the northeastern and middle SCS, respectively. In addition, generated mechanisms of those atmospheric responses are also analyzed.

9.2 Data and Methods

In this chapter, to identify the occurrences and distribution characteristics of CJEV and the Kuroshio intrusion, satellite data, including SST, sea surface height (SSH) and geostrophic currents, are used. Meanwhile, to evaluate the atmospheric responses to the Kuroshio modulation that takes place within the Luzon Strait, satellite-based sea surface winds (SSWs) and precipitation from Special Sensor Microwave Imager (SSM/I) are applied. In addition, to help the interpretation of possible mechanisms triggering the local atmospheric responses to the Kuroshio intrusion, the vertical velocity of air mass derived from reanalysis data are also used. Finally, for studying behavior of atmospheric responses to CJEV, numerical experiments based on Weather Research and Forecasting model (WRF) (WRF-ARW; http://www.wrf-model.org/index.php) are performed.

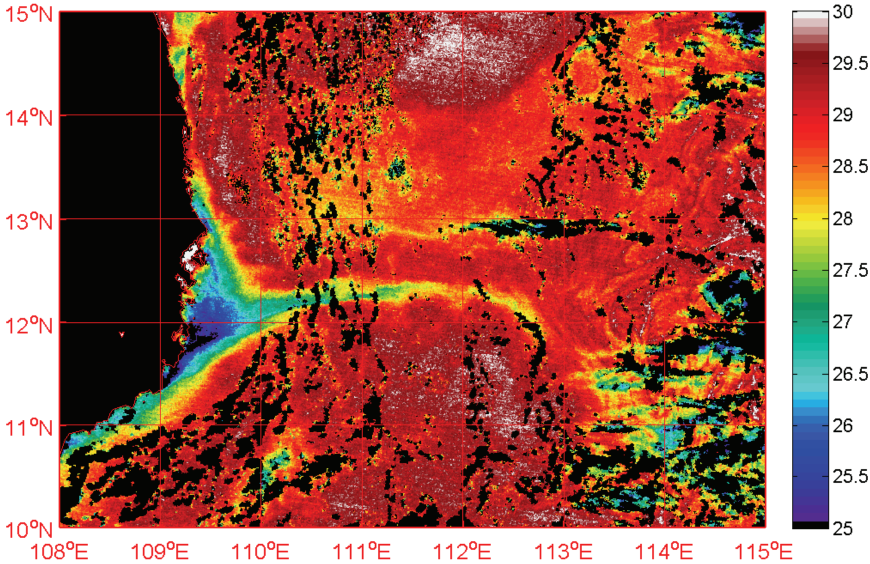

Fig. 9.3. MODIS SST image on 15 August 2014, showing an offshore coastal upwelling that occurred off the eastern coast of Vietnam.

9.2.1 *MODIS high resolution SST*

In this chapter, we use Moderate Resolution Imaging Spectroradiometer (MODIS) SST images from 2002 to 2014 to observe the offshore CJEV in summer. The spatial resolution is 1.1 km. Figure 9.3 shows an example, in which a CJEV with the lowest temperature of 25°C occurred at 12°N off the southeastern coast of Vietnam. The data are downloaded from http://oceancolor.gsfc.nasa.gov/ and processed by software SeaDAS version 6.4.

9.2.2 *SSH and geostrophic currents*

SSH and geostrophic currents are processed and provided by Archiving Validation and Interpretation of Satellite Data in Oceanography (AVISO). These products are merged data from altimeter-observed SSHs retrieved from Topex/Poseidon, ERS-1/2, Janson-1/2 and Envisat. They cover the range from 1993 to the present, with a $0.25^\circ \times 0.25^\circ$ spatial resolution (https://www.aviso.altimetry.fr/en/data/).

9.2.3 *SSW*

SSWs product used in this study is retrieved from sensor SeaWinds onboard QuikSCAT satellite. This dataset covers the range from July 1997 to November 2009, with a 0.25° spatial resolution. It can be downloaded from the web site of REMSS through http://www.remss.com/mission/qscat.

9.2.4 *SST*

The AVHRR Pathfinder version 5.2 SST data is used here to recognize the main pathway of the Kuroshio intrusion within the Luzon Strait. This product covers the period from November 1981 to December 2012, with a spatial resolution of 4 km (https://www.nodc.noaa.gov/SatelliteData/pathfinder4km/). In addition, only night-time data are used here.

9.2.5 *Precipitation from SSM/I*

The precipitation data are retrieved form SSM/I radiometer. The measured precipitation ranges from 0 to 25 mm/h. The data are available from July 1987 to the present. The product with a spatial resolution of $0.25^\circ \times 0.25^\circ$ is obtained from http://www.remss.com/missions/ssmi.

9.2.6 *Vertical velocity of atmosphere*

The data of vertical velocity of atmosphere are derived from ERA-Interim reanalysis data of European Center for Medium Range Weather Forecast (ECMWF). ERA-Interim provides daily or monthly data from January 1979 to the present. This product is used to evaluate the atmospheric responses (movement in the vertical) in response to occurrences of Kuroshio intrusion. Daily ERA-Interim data with spatial resolution $0.125^\circ \times 0.125^\circ$ are downloaded from http://apps.ecmwf.int/datasets/data/interim-full-daily/levtype=pl/.

9.2.7 *WRF atmospheric model*

Series of numerical experiments based on atmospheric WRF model are performed to evaluate the atmospheric responses to CJEV. Nested model domains are shown in Figure 9.4. Grid sizes are 4 and 12 km, respectively. Initial and lateral boundary conditions for WRF are retrieved

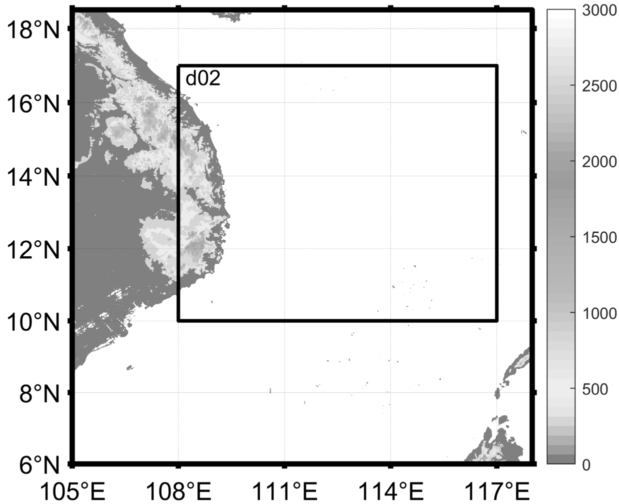

Fig. 9.4. WRF model domains, parent: 6–18.5°N, 105–118°E, resolution: 12 km; d02 (nested): 10–17°N, 108.5–117°E, resolution: 4 km. Gray shading shows the land topography.

from Global Forecast System FNL version global analysis field in a 6-hour temporal interval (1° × 1° spatial resolution) throughout a 138 h simulation from 00 UTC 5 August to 18 UTC 10 August 2009. Unified Noah land-surface model is used for land-surface process parameterization; planetary boundary layer parameterization is based on YSU scheme; and convective parameterization scheme is based on Kain–Fritsch scheme.

9.3 Impacts of Vietnam Coastal Upwelling to Atmospheric Environment

9.3.1 *Wind response*

Xie *et al.* [2003] demonstrated a marked relationship between the wind speed reduction and formation of regional cold filaments based on series of satellite observations. Here, we examine the possible linkage of atmospheric (wind) response to CJEV in a more direct approach. We execute two numerical experiments: standard experiment (EXP_{STD}: without CJEV) and contrast experiment (EXP_{CJ}: with CJEV), and attempt to reveal the effects of CJEV on the atmosphere.

For EXP_{CJ}, SST data with distinct CJEV (as shown in Figure 9.3) are interpolated onto the fine-grid model domain to recognize the boundary of CJEV. Later on, to compare with following experiments consistently and for simplification, isotherm of 27°C is defined as the boundary of CJEV, the temperature within (outside) the patch of CJEV is set to 26°C (30°C) uniformly. For the same reason, lower boundary condition in EXP_{STD} is replaced by spatially uniform 30°C to initialize the simulation. Except the configured background SST for different experiment scenarios, all other conditions and physical configurations of the two experiments are identical.

Figures 9.5(a) and 9.5(b) show the atmospheric response of low-level wind forcing (arrows, in knots) and lower boundary condition of SST (°C) at 18:00 UTC, 10 August 2009, simulated in both experiments. For a first approximation, both scenarios show similar situations, except the cold patch (from SST) attached along the southeastern coast of Vietnam. Furthermore, Figure 9.5(c) shows the difference between EXP_{CJ} and EXP_{STD}. Differenced wind forcing is shown in arrows ($m\,s^{-1}$), differenced temperature in color shading (°C) and contours denoted the differenced wind speed ($m\,s^{-1}$). With difference, many interesting scenarios are revealed. It is evident that, with the influence of cold patch, the difference of direct wind modulation and reduction of wind speed attain $3\,m\,s^{-1}$ (about 33% of the original magnitude, arrows in Figure 9.5(c)) and $2.5\,m\,s^{-1}$ (see contours in Figure 9.5(c)), respectively.

9.3.2 *Possible linkage between wind response and CJEV*

After revealing the positive SST–SSW relationship between upwelling-driven cold patch and the atmospheric response of wind reduction over CJEV, we aim to resolve the physical linkage between CJEV and consequential wind forcing modulation.

Previous studies pointed out that wind modulation to SST change can result from pressure gradient force or modulated vertical momentum flux [Lindzen and Nignam, 1987; Wallace *et al.*, 1989; Hayes *et al.*,1989; Small *et al.*, 2005]. Lindzen and Nigam [1987] (L&N87) proposed that the SST variation induces direct changes in the air temperature above and consequentially causes a pressure change in the atmosphere. Later on, through hydrostatic balance, low-level winds would diverge onto cold SST patches and converge onto warm SST patches.

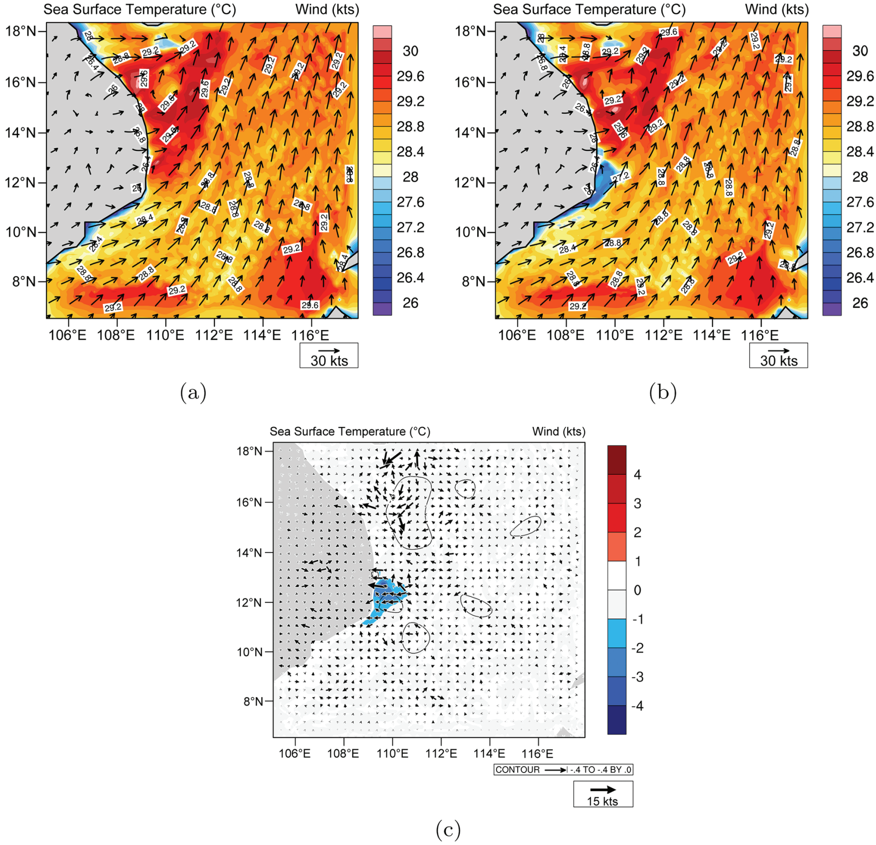

Fig. 9.5. Lower boundary conditions (°C) in (a) EXP_{STD} and (b) EXP_{CJ}. Vectors denote wind forcing (knots) of bottom layer in two experiments. (c) Difference between (a) and (b). Contours in (c) show the reduction of wind forcing (in m s^{-1}).

Source: Redrawn from Zheng *et al.* [2016].

On the other hand, Wallace *et al.* [1989] (Wa89) investigated the effect of SST gradient on surface winds occurring in the eastern Tropical Pacific and demonstrated that the meridional component of the trade wind is highly associated with the lower SST in the cold tongue on seasonal and interannual time scales. Wa89 explained that this is because the high winds aloft are decoupled from surface winds due to the presence of more stable stratification over colder SST.

Subsequently, the increased stratification in the boundary layer limits the transfer of vertical heat and momentum fluxes. Thus, the lower layer becomes less aware of the variation in the layer aloft, resulting in a "decoupling condition". On the contrary, the boundary layer is less stable over warmer SST. Because it induces stronger vertical mixing and reduction of vertical wind shear, it eventually leads to a more uniform velocity profile with higher winds at the sea surface relative to that over cold SST.

Figure 9.6 shows difference between EXP_{CJ} and EXP_{STD} (EXP_{CJ}–EXP_{STD}), indicating the low-level divergence field. One can see that positive divergence anomaly matches well with the upwelling (cooling) region, which is consistent with the theory of L&N87 that low-level winds would diverge onto cold SST patches. However, it is worth noting that this process is insufficient to explain the uniform onshore modulations over the cold patch off eastern coast of Vietnam (as shown in Figure 9.5(c)).

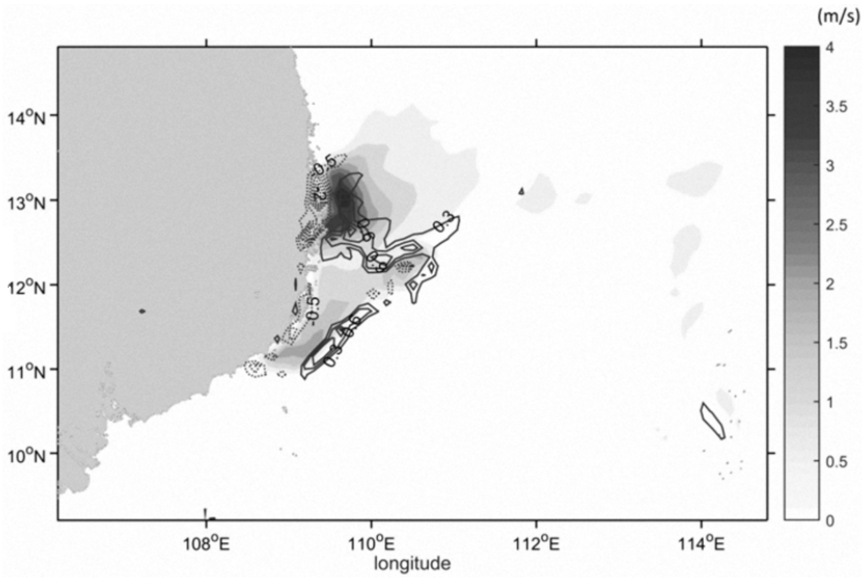

Fig. 9.6. Model simulated modulation of low-level horizontal divergence field (below 200 m, solid contours: divergence, dashed contours: convergence) and modulation of wind speed (gray scaling, $m\,s^{-1}$).

Source: Redrawn from Zheng *et al.* [2016].

Meanwhile, it is evident that a distinct convergence zone appeared along the coastline of eastern Vietnam (near offshore upwelling region). This suggests that the existence of the land–sea boundary might play a certain role in triggering the possible convection across the land–sea interface and thus cause the subsequent unusual onshore wind modulation in the bottom boundary layer. Figure 9.6 also shows a comparison between wind speed modulation (gray scaling) and divergence/convergence fields (contours). One can see that the most apparent wind modulations occur between the areas where strongest divergence and convergence take place (seeing solid and dashed contours in Figure 9.6). The result shows very good consistency with a classic vertical convection scenario that modulated wind, as a portion of the complete convection, would appear between convergence and divergence zones.

Meanwhile, according to Wa89, possible wind reduction results from the decoupling of low-level winds from the high winds aloft (prevailing southwest monsoon in our background environment), in the presence of more stable stratification (e.g., suppressed vertical mixing and stronger wind shear in the vertical) over colder SST. Figure 9.7 shows the wind velocity profiles at different levels sampled at the center of the upwelling region ($\sim$109.7°E, 12.5°N) in EXP_{STD} and EXP_{CJ}. Black arrows show the difference between both experiments (EXP_{CJ}–EXP_{STD}). Referring to Figure 9.7, it is evident that a relatively distinct decoupling of high winds aloft from surface winds (enhancement of vertical wind shear) can be seen in EXP_{CJ}, relative to EXP_{STD}. This result reproduces the scenario suggested by Wa89 that wind reduction resulted from suppressed vertical mixing due to presence of more stable stratification over colder SST. Definitely, in our case, the colder SST has resulted mainly from the coastal upwelling.

Furthermore, in Figure 9.7, interestingly, the wind modulation (EXP_{CJ}–EXP_{STD}) near the sea surface points to almost due west (consistent with the result shown in Figure 9.5(c)) instead of the opposite direction of prevailing southwest monsoon. Referring back to Wa89, the wind modulation should point exactly to the opposite direction of original prevailing monsoon, because lower sea surface wind speed related to colder SST is due mainly to a stronger stratification and a more stable boundary layer leading to a decoupling of low-level winds from the high winds aloft. However, in Figure 9.7, the wind modulation in the bottom level is flowing westward, and turning eastward in the upper level (150 m). The difference in vertical wind profile between EXP_{STD} to EXP_{CJ} identifies a vertically inverse wind modulation associated with presence of CJEV. Overall, Figures 9.6 and 9.7

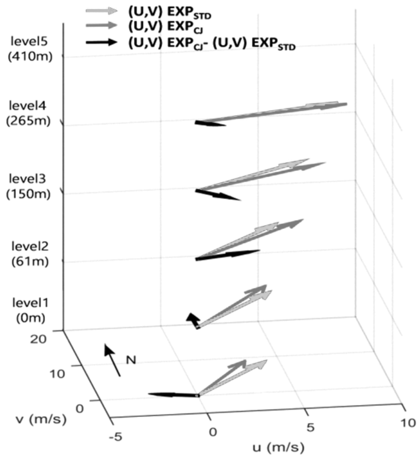

Fig. 9.7. Wind velocity vectors at different levels. Differenced wind velocities (modulations) are obtained by calculating the difference between two experiments (EXP$_{CJ}$–EXP$_{STD}$).

infer that as per mechanisms raised by L&N87 and Wa89, modulation of wind plays a certain role in the upwelling within this region. Nevertheless, there must be a different process dominating the significant onshore wind modulations, which might imply the importance of land–sea discrepancy within the boundary layer.

To further clarify the possible mechanism, therein, daily composite of vertical velocity field (w, cm s^{-1}) and horizontal wind modulations (vectors, in knots) in the bottom atmospheric layer are processed. Figure 9.8 shows the differenced vertical velocity (EXP$_{CJ}$–EXP$_{STD}$), from which one can see that there is a distinctly vertical uplift revealing along the land–sea boundary of the southeastern coast of Vietnam. It is worth noting that this uplift shows perfect consistency with the convergence zone of wind modulations over CJEV (see arrows in Figure 9.8). Meanwhile, because of the modulated onshore winds blowing from the sea to the land directly across the coastline (land–sea boundary), a distinctly vertical uplift appears over the land accompanying the convergence zone of onshore wind modulations in the bottom atmospheric layer. The coincidence demonstrated in Figure 9.8 leads us to the possible scenario of sea breeze.

To examine the possible role played by sea breeze on the wind modulation in response to CJEV, we focus on the dominant daily signal. Figure 9.9(a) shows the divergence of hourly-averaged surface wind along a zonal section (12.5°N) roughly perpendicular to the coast in standard

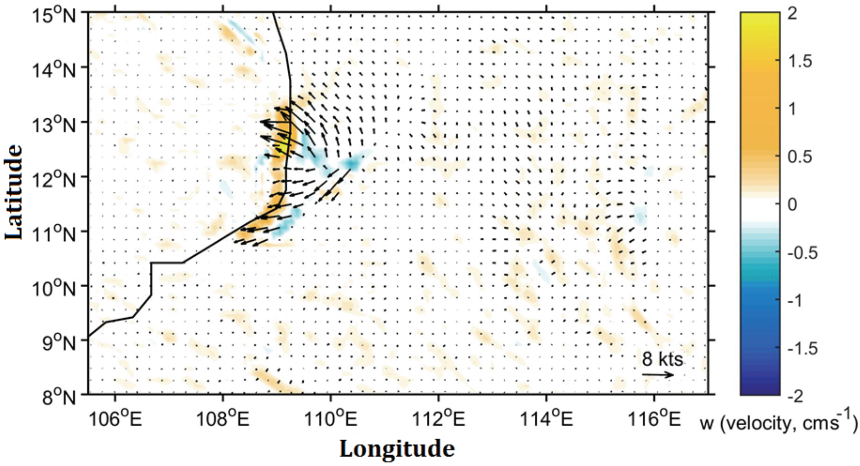

Fig. 9.8. Daily-composite of modulations of vertical movement velocity (color shading, in $cm\,s^{-1}$) and wind forcing (vectors, in knots) in the bottom-layer of atmospheric model. Modulations are obtained by calculating the difference between experiments EXP_{CJ} and EXP_{STD}. *Source*: Redrawn from Zheng *et al.* [2016].

experiment (EXP_{STD}, white contours). The deviation of wind divergence from EXP_{STD} to EXP_{CJ} is superimposed on the figure with color shadings.

One can see that in EXP_{STD}, surface wind divergence takes place in the ocean and convergence occurs over the land region. Furthermore, the convergence over land region is significantly stronger than that over ocean region. In particular, its strength increases from morning to afternoon and attains the maximum at around 2:00 pm, decreasing gradually till midnight. This scenario implies a typical sea breeze process.

On the other hand, Figure 9.9(b) shows a vertical profile along 12.5°N of the deviated low-level U-velocity at 2:00 pm. It is evident that a significantly anomalous easterly wind occurs in the low-level (below 200 m) coastal area accompanied by velocity inversion above 200 m. Both Figures 9.8 and 9.9 demonstrate an intensification of the sea breeze circulation, when the cold patch exists. This suggests that the sea breeze process is the key mechanism for triggering the shoreward wind modulations, as shown in our previous analyses.

Since the land is warmer than the sea during the day, the local surface wind blows from the sea to the land. Consequently, the sea breeze circulation occurs due to the horizontal temperature difference between the land and the sea. Meanwhile, the circulation is opposite

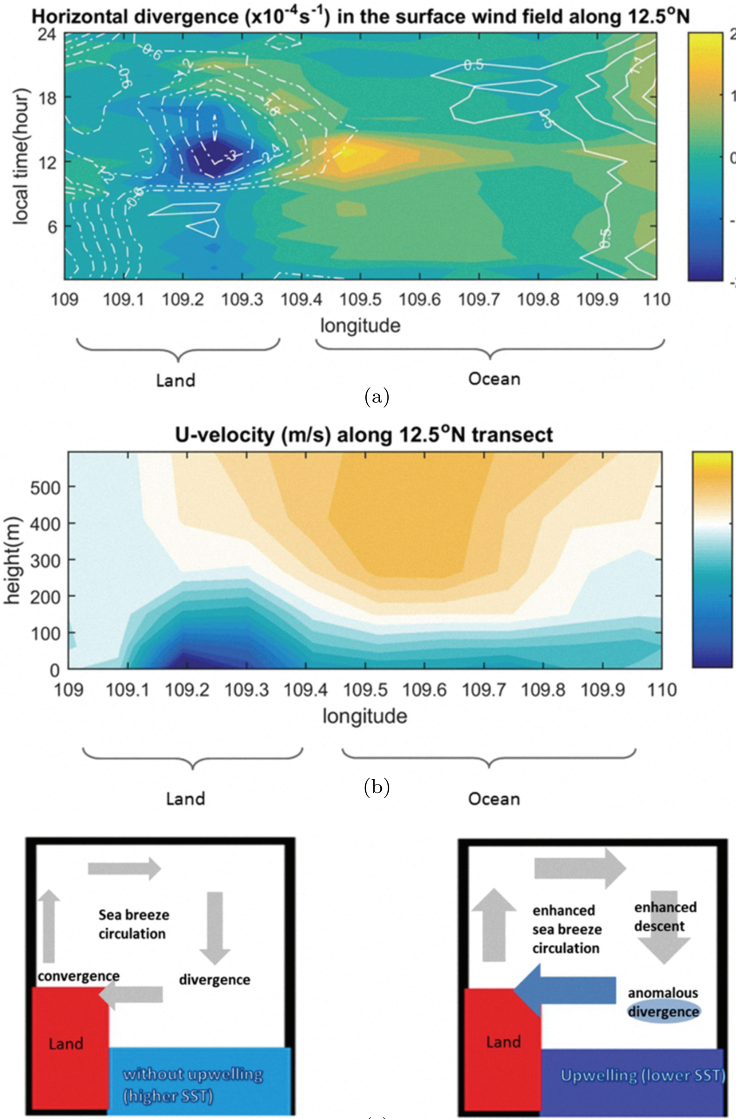

Fig. 9.9. (a) Hourly averaged surface wind divergence along zonal section (12.5°N) in the EXP_{STD}. The deviation of divergence between EXP_{STD} and EXP_{CJ} is shown shaded. (b) Modulation of the U-component wind along a 12.5°N transect. (c) Schematics corresponding to normal sea breeze and enhancement of onshore sea breeze (across the land–sea boundary) due to lower SST carried by coastal upwelling.

Source: Redrawn from Zheng *et al.* [2016].

at night. Thus, the sea breeze circulation may be stronger once coastal upwelling is present, because the negative SST anomaly enhances the horizontal temperature difference between the land and sea [Franchito *et al.*, 1998]. On the other hand, the effect of land breeze might weaken, because the temperature difference between land and sea is reduced, given the same situation of lower SST induced by coastal upwelling.

Synergy of aforementioned two-way mechanisms would trigger a completely enhanced sea breeze circulation and thus a distinct onshore wind modulation, as shown in the case of CJEV. Because the contrast between the land and the sea increases largely due to the extra contribution resulted from strong coastal upwelling. Schematics of aforementioned processes are shown in Figure 9.9(c). Overall, since the sea/land breeze is a pressure- (density-)driven circulation, the influence of sea breeze on the modulation of coastal wind over upwelling region might be considered as a special case of the mechanism proposed by L&N87.

Finally, to evaluate the robustness of the impact of sea breeze effect on the local wind system off eastern mid-Vietnam, raised in previous sections, a long-term composite of wind modulation corresponding to all CJEV events during available Advanced Scatterometer (ASCAT) data for the period (2007–2015) is processed (Figure 9.10). It is worth noting that this evidence is totally observations-based, which is independent of our simulated results. The results show that observation-based results also show an anomalous westerly wind modulation appearing over the strong upwelling region, which shows good consistency with simulated results. This composite can be served as an independent evidence for further supporting the scenario concluded from our numerical experiments.

9.4 Influence of the Kuroshio Intrusion on the Local Atmosphere

Another story included in this chapter is the relationship between distinct ocean dynamic features, i.e., Kuroshio intrusions, and consequential atmospheric responses. To approach the main target of this topic, all the Kuroshio intrusion events are collected for analysis to clarify the relationship of the Kuroshio intrusions to consequential atmospheric responses.

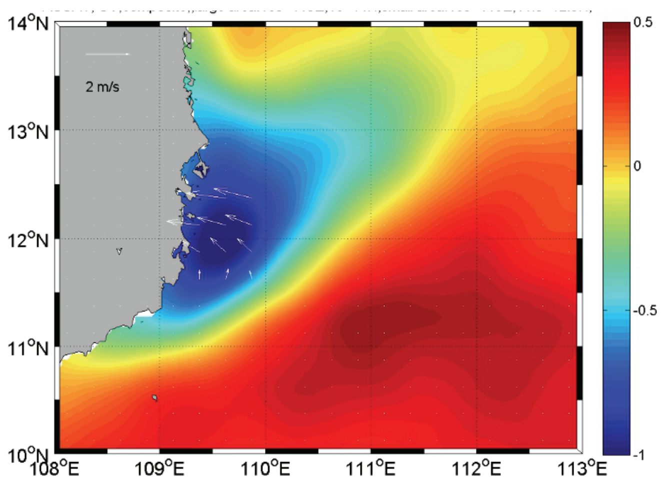

Fig. 9.10. Long-term composite of wind modulation (based on ASCAT data, http://manati.star.nesdis.noaa.gov/datasets/ASCATData.php) and SST deviation (unit: °C, made by GHRSST, http://cersat.ifremer.fr/data/collections/ghrsst) corresponding to all CJEV events (defined by SST drop >1.5°C than surrounding background region) during available ASCAT data period (2007–2015).

Source: Redrawn from Zheng *et al.* [2016].

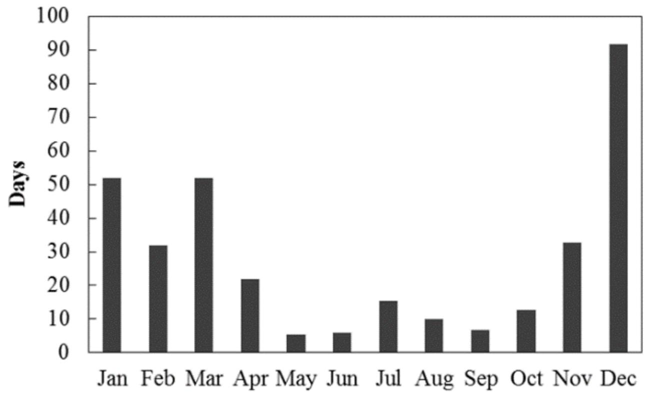

Fig. 9.11. Monthly distribution of the Kuroshio intrusion events (in days) that occurred during 2000–2009.

The Kuroshio intrusion event is defined based on the geostrophic current speed method proposed by Liang *et al.* [2003]. Based on the definition of Kuroshio intrusion, the monthly distribution characteristics of the Kuroshio intrusion events (in days) based on SSH and geostrophic currents are shown in Figure 9.11. One can see that the Kuroshio intrusion occurs most frequently from November to April of the following year. This result is generally consistent with the results documented in previous studies, which pointed out that southwest monsoon in summer provides an unfavorable environment for the Kuroshio intrusion occurrence [Wang and Chern, 1987; Shaw, 1991].

To further understand the possible impact of the Kuroshio intrusion on the local atmosphere, we process related composited images based on all the Kuroshio intrusion events identified in the previous section. As shown in Figure 9.12(a), composite SSH image and geostrophic currents show

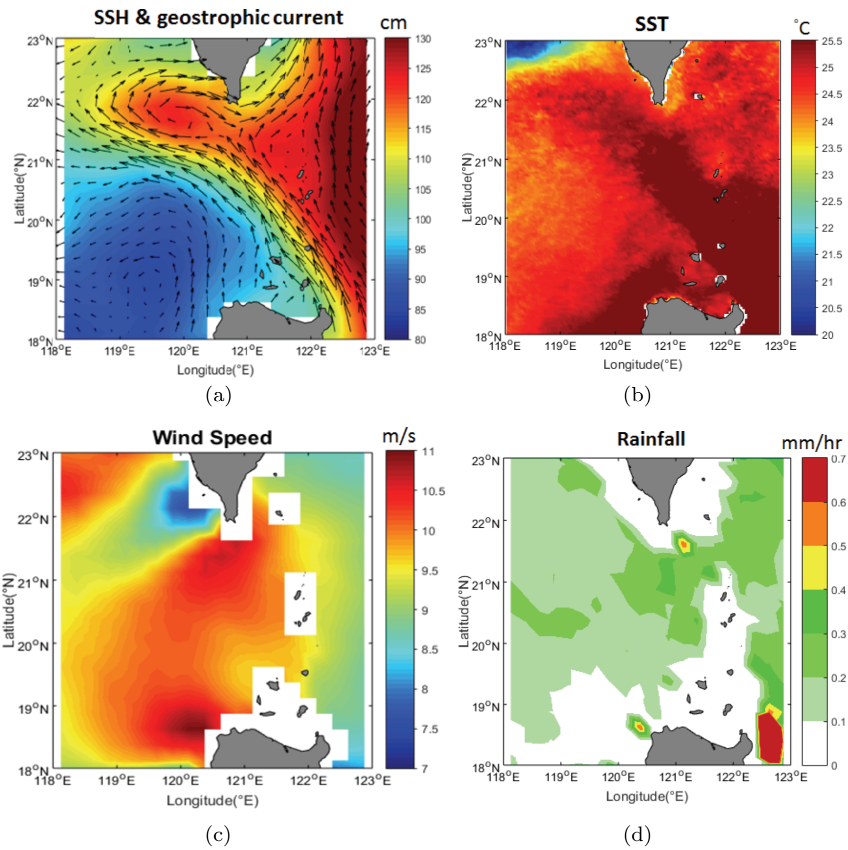

Fig. 9.12. Composite images of (a) SSH (cm) and geostrophic currents, (b) SST (°C), (c) sea surface wind speed (m s^{-1}) and (d) rainfall (mm/h) corresponding to all the Kuroshio intrusion events occurring in the period from November to April during 2000–2009.

typical Kuroshio intrusion patterns. Meanwhile, composited SST image in Figure 9.12(b) shows consistent patterns of the higher SST imagery appearances along the main path of the Kuroshio intrusion entering the northern SCS. SSWs in Figure 9.12(c) show spatially ununiformed distribution patterns. It is evident that winds are relatively stronger over the Luzon Strait. This situation very likely results from interaction of topography and northeast monsoon prevailing in boreal winter. The rainfall patterns in Figure 9.12(d) seem to show a different scenario. Heavy rainfall imagery centered at east Luzon Island and southeastern corner of Taiwan Island does not coincide with "the Kuroshio intrusion mode" patterns as shown in Figures 9.12(a)–9.12(c).

As aforementioned, the above composite image patterns are very likely resulting from contribution of northeast monsoon prevailing in boreal winter (see Figure 9.13). To further clarify the physical linkages of the Kuroshio intrusion to consequential atmospheric responses, we remove the Kuroshio

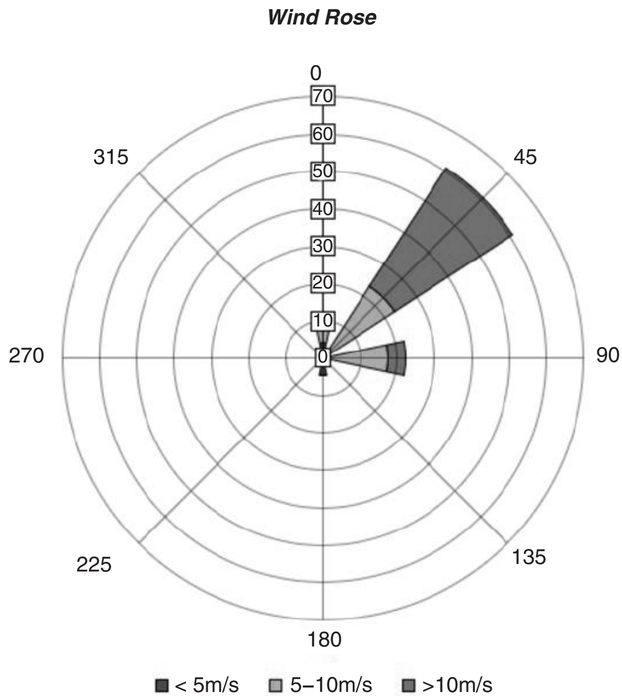

Fig. 9.13. Sea surface wind rose patterns derived from all the Kuroshio intrusion events from 2000 to 2009.

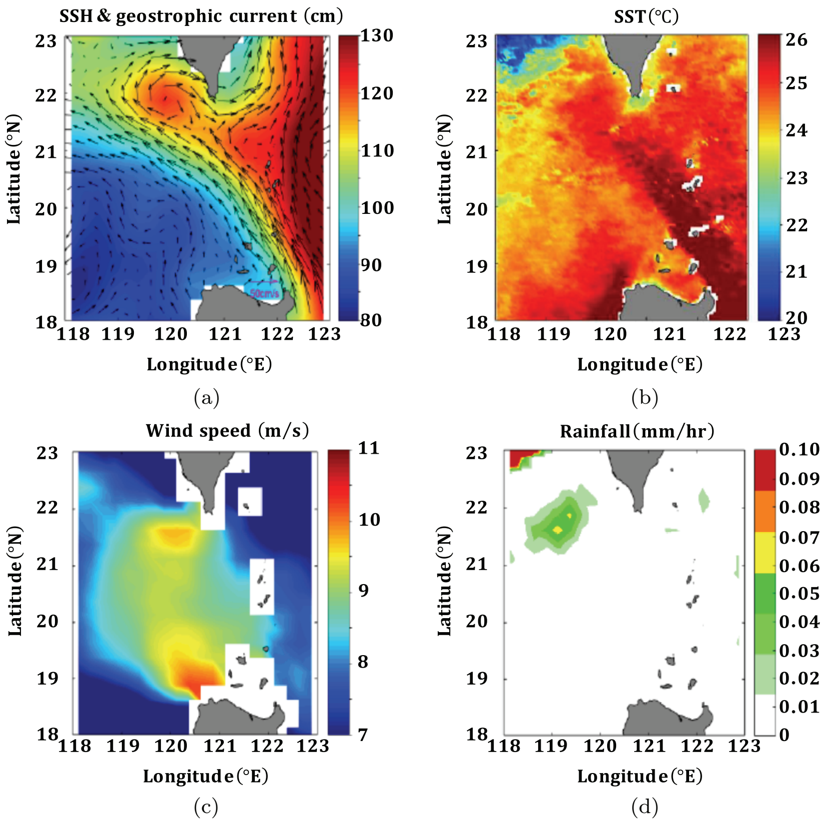

Fig. 9.14. Composite images of (a) SSH (cm) and geostrophic currents, (b) SST (°C), (c) sea surface wind speed ($m\,s^{-1}$) and (d) rainfall (mm/h) corresponding to all the Kuroshio intrusion events without strong northeast monsoon.

intrusion events occurring during peak northeast monsoon season and produce new composite images using the remaining Kuroshio intrusion events. The results are shown in Figures 9.14(a)–9.14(d).

One can see that the SSH and SST images in Figures 9.14(a) and 9.14(b) still show the typical Kuroshio intrusion patterns. Sea surface wind image in Figure 9.14(c) shows dominant east-westward wind forcing patterns. However, what is more interesting is that the rainfall image in Figure 9.14(d) shows a positive anomaly of 11.5 mm/event (under the assumption that a Kuroshio intrusion event persists 8 days). This suggests an interesting scenario that Kuroshio intrusion causes not only a positive SST anomaly within the Luzon Strait (due to Kuroshio intrusion bringing

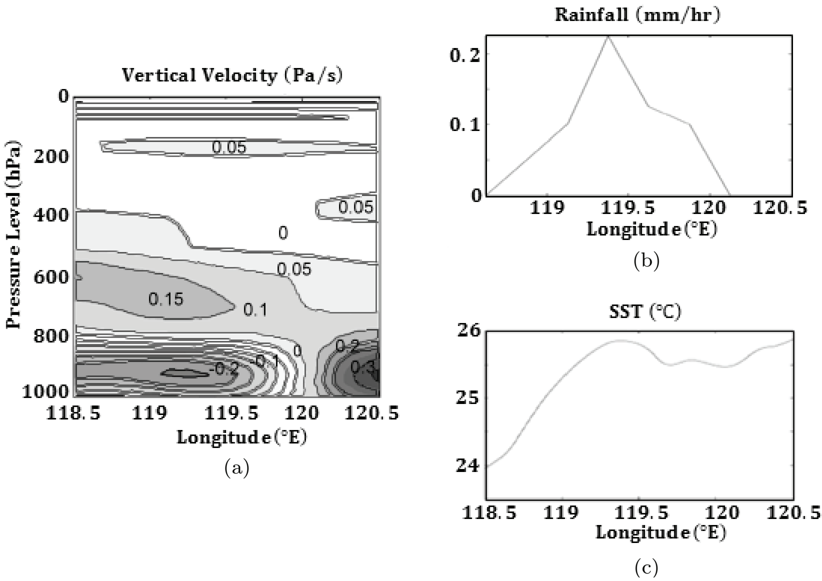

Fig. 9.15. (a) Vertical velocity distribution along 22°N between 118.5°E and −120.5°E, (b) rainfall and (c) SST along 22°N corresponding to the distinct Kuroshio intrusion event that occurred in March 2005.

warmer Kuroshio water into the Luzon Strait) but also a precipitation anomaly, which might modify local mass and salinity exchange and in other ways impact the regional weather system. Nevertheless, more evidences are needed to document the relationship and physical linkage therein.

The above analysis results bring out possible linkages between temperature, precipitation responses and the Kuroshio intrusion, i.e., the SST anomaly caused by the Kuroshio intrusion may trigger local precipitation response through certain aero-dynamic processes [Chow *et al.*, 2015; Zheng *et al.*, 2016]. For further understanding the causal-linkage therein, Figure 9.15(a) shows the vertical velocity of atmosphere, which is retrieved from ERA-Interim reanalysis data along 22°N and between 118.5°E and 120.5°E, corresponding to a distinct Kuroshio intrusion event that occurred in March 2005. One can see that uplift of atmosphere took place mainly from the sea surface to height of 850 hPa at 118.5–120°E. The maximum uplift occurred at 119–119.5°E and height of 900 hPa. The uplift speed reaches 0.2 Pa per second. Figure 9.15(b) shows that the heaviest precipitation (>50 mm/event) was centered at 119–119.5°E. It is evident that the strongest uplift air-flow shows great agreement with the heaviest precipitation. In addition, both of the strongest uplift of atmosphere and precipitation take place where the SST gradient attains a maximum as shown in Figure 9.15(c).

Overall, aforementioned analyses show that the strongest uplift of lower layer atmosphere from the sea surface to a height of 850 hPa and the heaviest precipitation agree well with the distribution positions of the highest SST, while a marked Kuroshio intrusion event occurred. L&N87 indicated that the SST variation causes direct changes in the air temperature above and thus a pressure change in the atmosphere. Later on, low-level winds converge onto warm SST patches (upward movement of atmosphere over the patch) and diverge onto cold SST patches, due to hydrostatic balance. This supports the interpretation of the process that Kuroshio intrusion brings warmer Kuroshio water into the Luzon Strait (most marked off southwest of the Taiwan Island), and thus causes consequential atmospheric convection and heavy precipitation eventually.

9.5 Summary

Based mainly on satellite observations, this chapter investigates possible regional atmospheric responses to two distinct dynamic features appearing within the SCS: the Kuroshio intrusion within the Luzon Strait and the northeastern SCS, and the distinct upwelling driven cool-jet located at the middle SCS off the eastern coast of Vietnam, respectively. By satellite observations, numerical experiments, and theoretical analysis, characteristics, progresses and generated mechanisms of atmospheric responses to those two distinct dynamic features in the SCS are preliminarily unveiled. The results of this chapter shed new light onto the linkage between atmosphere and hydrosphere on a regional scale. More interesting works related to interactions across the air–sea interface and the consequential impacts resulting from those interactions back to the regional weather system, ocean environment and ecosystem are highly expected.

Acknowledgments

This work was supported by the Ministry of Science and Technology Taiwan, through grants MOST 104-2611-M-003-003 and MOST 105-2611-M-003-003. We thank Mr. Yan-Hao Chao for his help in SeaDAS data processing and WRF experiments.

References

Anthes, R. A. (1978). The height of the planetary boundary layer and production of the circulation in a sea-breeze model, *J. Atmos. Sci.*, 35, pp. 1231–1239.

Caruso, M. J., Gawwarkiewicz, G. G. and Beardsley, R. C. (2006). Interannual variability of the Kuroshio intrusion in the South China Sea, *J. Oceanogr.*, 62, pp. 559–575.

Chelton, D. B. and Xie, S. P. (2010). Coupled ocean-atmosphere interaction at oceanic mesoscales, *Oceanogr.*, 23 (4), pp. 52–69.

Chen, G. X., Hou, Y. J. and Chu, X. Q. (2011). Water exchange and circulation structure near the Luzon Strait in early summer, *Chin. J. Oceanol. Limn.*, 29 (2), pp. 470–481.

Chow, C. H., Liu, Q. and Xie, S. P. (2015). Effects of Kuroshio Intrusions on the atmosphere northeast of Taiwan Island, *Geophys. Res. Lett.*, 42 (5), pp. 1465–1470.

Farris, A. and Wimbush, M. (1996). Wind-induced Kuroshio intrusion into the South China Sea, *J. Oceanogr.*, 52, pp. 771–784.

Franchito, S. H., Rao, V. B., Stech, J. L. and Lorenzzetti, J. A. (1998). The effect of coastal upwelling on the sea-breeze circulation at Cabo Frio, Brazil: A numerical experiment, *Ann. Geophys.*, 16, pp. 866–871.

Frenger, I., Gruber, N., Knutti, R. and Münnich, M. (2013). Imprint of Southern Ocean eddies on winds, clouds and rainfall, *Nat. Geosci.*, 6, pp. 608–612.

Gong, G. C., Liu, K. K., Liu, C. T. and Pai, S. C. (1992). The chemical hydrography of the South China Sea west of Luzon and a comparison with the west Philippine Sea, *Terr. Atmos. Ocean. Sci.*, 3 (4), pp. 587–602.

Hayes, S. P., McPhaden, M. J. and Wallace, J. M. (1989). The influence of sea surface temperature on surface wind in the eastern equatorial Pacific: Weekly to monthly variability, *J. Clim.*, 2, pp. 1500–1506.

Ho, C. R., Kuo, N. J., Zheng, Q. and Soong, Y. S. (2000). Dynamically active areas in the South China Sea detected from TOPEX/POSEIDON satellite altimeter data, *Remote Sens. Environ.*, 71, pp. 320–328.

Hsin, Y. C., Wu, C. R. and Chao, S. Y. (2012). An updated examination of the Luzon Strait transport, *J. Geophys. Res.*, 117 (C3), C03022, http://dx.doi.org/10.1029/2011JC007714.

Kousky, V. E. (1980). Diurnal rainfall variability in Northeast Brazil, *Mon. Weather Rev.*, 108, pp. 488–498.

Kuehl, J. J. and Sheremet, V. A. (2009). Identification of a cusp catastrophe in a gap-leaping western boundary current, *J. Mar. Res.*, 67, pp. 25–42.

Kuo, N. J., Zheng, Q. and Ho, C. R. (2000). Satellite observation of upwelling along the western coast of the South China Sea, *Remote Sens. Environ.*, 74, pp. 463–470.

Kuo, N. J., Zheng, Q. and Ho, C. R. (2004). Response of Vietnam coastal upwelling to the 1997–1998 ENSO event observed by multi-sensor data, *Remote Sens. Environ.*, 89, pp. 106–115.

Liang, W. D., Tang, T. Y., Yang, Y. J., Ko, M. Y. and Chung, W. S. (2003). Upper-ocean current around Taiwan, *Deep Sea. Res., Part II*, 50, pp. 1085–1105.

Lindzen, R. S. and Nigam, S. (1987). On the role of sea surface temperature gradients in forcing low-level winds and convergence in the tropics, *J. Atmos Sci.*, 44 (17), pp. 2418–2436.

Lu, R. and Turco, R. P. (1994). Air pollutant transport in a coastal environment. Part 1: Two-dimensional simulations of sea-breeze and mountain effects, *J. Atmos. Sci.*, 51, pp. 2285–2308.

Metzger, E. J. and Hurlburt, H. E. (1996). Coupled dynamics of the South China Sea, the Sulu Sea, and the Pacific Ocean, *J. Geophys. Res.*, 101 (C5), pp. 12331–12352.

Metzger, E. J. and Hurlburt, H. E. (2001). The nondeterministic nature of Kuroshio penetration and eddy shedding in the South China Sea, *J. Phys. Oceanogr.*, 31, pp. 1712–1732.

Nan, F., Xue, H. and Yu, F. (2015). Kuroshio instruction into the South China Sea: A review, *Prog. Oceanogr.*, 137, pp. 314–333.

Nan, F., Xue, H. Chai, F. Shi, L. Shi, M. and Guo, P. (2011). Identification of different types of Kuroshio intrusion into the South China Sea, *Ocean Dyn.*, 61 (9), pp. 1291–1304, http://dx.doi.org/10.1007/s10236-011-0426-3.

Nitani, H. (1972), Beginning of the Kuroshio, in H. Stommel and K. Yoshida (Eds.), *Kuroshio Its Physical Aspects*, University of Tokyo Press, Tokyo, pp. 129–163.

Oey, L. Y., Chang, M. C., Huang, S. M., Lin, Y. C. and Lee, M. A. (2015). The influence of shelf-sea fronts on winter monsoon over East China Sea, *Clim. Dyn.*, 45 (7–8), pp. 2047–2068, doi:10.1007/s00382-014-2455-3.

Shaw, P. T. (1991). The seasonal variation of the intrusion of the Philippine sea water into the South China Sea, *J. Geophys. Res.*, 96, pp. 821–827.

Small, R. J., Xie, S. P. and Hafner, J. (2005). Satellite observations of mesoscale ocean features and copropagating atmospheric surface fields in the tropical belt, *J. Geophys. Res.*, 110, C02021, doi:10.1029/2004JC002598.

Wallace, J. M., Mitchell, T. P. and Deser, C. (1989). The influence of sea surface temperature on surface wind in the eastern equatorial Pacific: Seasonal and interannual variability, *J. Clim.*, 2, pp. 1492–1499.

Wang, J. and Chern, C. S. (1987). The warm-core eddy in the northern South China Sea. Part I: Preliminary observations on the warm-core eddy, *Acta Oceanogr Taiwanica*, 18, pp. 92–103.

Wang, Y., Fang, G., Wei, Z., Qiao, F. and Chen, H. (2006). Interannual variation of the South China Sea circulation and its relation to El Niño, as seen from a variable grid global ocean model, *J. Geophys. Res.*, 111, C11S14.

Wu, C.-R. and Hsin, Y. C. (2012). The forcing mechanism leading to the Kuroshio intrusion into the South China Sea, *J. Geophys. Res.*, 117 (C7), C07015, http://dx.doi.org/10.1029/2012JC007968.

Xie, S. P. (2004). Satellite observations of cool ocean-atmosphere interaction, *Bull. Am. Meteorol. Soc.*, 85 (2), pp. 195–208, doi:10.1175/BAMS-85-2-195.

Xie, S. P., Chang, C. H., Xie, Q. and Wang, D. (2007). Intraseasonal variability in the summer South China Sea: Wind jet, cold filament, and recirculations, *J. Geophys. Res.*, 112, C10008, doi:10.1029/2007JC004238.

Xie, S. P., Xie, Q., Wang, D. X. and Liu, W. T. (2003). Summer upwelling in the South China Sea and its role in regional climate variations, *J. Geophys. Res.*, 108 (C8), 3261, doi:10.1029/2003JC001867.

Zheng, Z. W., Zheng, Q., Kuo, Y. C., Gopalakrishnan, G., Lee, C. Y., Ho, C. R., Kuo, N. J. and Huang, S. J. (2016). Impacts of coastal upwelling off east Vietnam on the regional winds system: An air-sea-land interaction, *Dyn. Atmos. Oceans*, 76, pp. 105–115.